Joule

CellPress

Article

Shallow Iodine Defects Accelerate the Degradation of α-Phase Formamidinium Perovskite

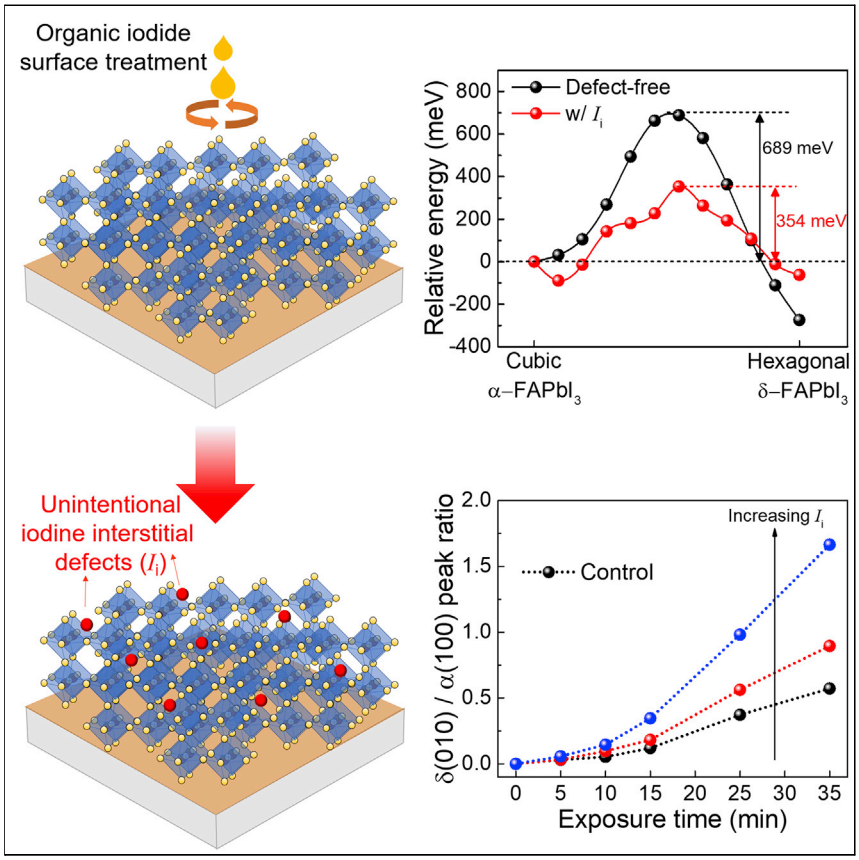

Systematic experimental and computational studies revealed that iodine interstitial defects (I_i) can be unintentionally generated during commonly used post-fabrication surface treatments for state-of-the-art perovskite solar cells (PSCs). Although shallow, I_i lowers the cubic-to-hexagonal phase transformation activation energy barrier of $FAPbI_3$-based perovskites to aggravate its instability. We propose a universal strategy to simultaneously avoid I_i generation and for more effective iodine vacancy passivation to realize PSCs that retain over 90% of their initial performance after near 1,000 h of continuous illumination.

Shaun Tan, Ilhan Yavuz, Marc H. Weber, ..., Kung-Hwa Wei, Jin-Wook Lee, Yang Yang

ilhan.yavuz@marmara.edu.tr (I.Y.)
jw.lee@skku.edu (J.-W.L.)
yangy@ucla.edu (Y.Y.)

HIGHLIGHTS

Perovskite surface treatment generates shallow iodine interstitial defects (I_i)

I_i aggravates the instability of $FAPbI_3$ perovskites

Universal strategy to avoid I_i generation and iodine vacancy passivation

Over 90% of initial performance retained after near 1,000 h of illumination

Tan et al., Joule 4, 2426–2442
November 18, 2020
https://doi.org/10.1016/j.joule.2020.08.016

CellPress

Joule

Article

Shallow Iodine Defects Accelerate the Degradation of α-Phase Formamidinium Perovskite

Shaun Tan,[1] Ilhan Yavuz,[2,*] Marc H. Weber,[3] Tianyi Huang,[1] Chung-Hao Chen,[1,4] Rui Wang,[1] Hao-Cheng Wang,[1,4] Jeong Hoon Ko,[5] Selbi Nuryyeva,[1] Jingjing Xue,[1] Yepin Zhao,[1] Kung-Hwa Wei,[4] Jin-Wook Lee,[6,*] and Yang Yang[1,7,*]

SUMMARY

Shallow defects are mostly benign in covalent semiconductors, such as silicon, given that they do not constitute non-radiative recombination sites. In contrast, the existence of shallow defects in ionic perovskite crystals might have significant repercussions on the long-term stability of perovskite solar cells (PSCs) because of the metastability of the ubiquitous formamidinium lead triiodide ($FAPbI_3$) perovskite and the migration of charged point defects. Here, we show that shallow iodine interstitial defects (I_i) can be generated unintentionally during commonly used post-fabrication treatments, which can lower the cubic-to-hexagonal transformation barrier of $FAPbI_3$-based perovskites to accelerate its phase degradation. We demonstrate that concurrently avoiding the generation of I_i and the more effective passivation of iodine vacancies (V_I) can improve the thermodynamic stability of the films and operational stability of the PSCs. Our most stable PSC retained 92.1 % of its initial performance after nearly 1,000 h of continuous illumination operational stability testing.

INTRODUCTION

The record power conversion efficiencies (PCEs) of single-junction metal halide perovskite solar cells (PSCs) have catapulted to over 25% in just over a decade.[1–5] With attainable PCEs now rivaling that of mature photovoltaic technologies based on conventional inorganic semiconductors, the attention of the community has turned to address the notorious instability issues of PSCs.

Shallow defects, by definition, do not constitute non-radiative recombination centers because of their low transition energies and are, therefore, considered mostly benign and of less importance in inorganic covalent semiconductors, such as silicon or gallium arsenide. In contrast, due to the characteristic ionic nature of metal halide perovskites, intrinsic point defects are charged,[6–8] and this has significant implications on its defect physics. Particularly, the migration of charged defects in response to a potential gradient is known to seriously degrade the long-term operational stability of PSCs.[9–12] Notably, several shallow defects are theoretically predicted to have low formation and migration activation energies.[6,7,9,12,13] This implies the possible generation of shallow defects during film fabrication and post-treatment processes. Although the initial device photovoltaic performance is mostly unaffected by the generated defects due to their shallow nature, the long-term

Context & Scale

Shallow defects, by definition, do not constitute non-radiative recombination centers and are, therefore, mostly benign and of less importance in inorganic covalent semiconductors, such as silicon or gallium arsenide. Perhaps, for this reason, shallow defects have received comparatively less attention from the metal halide perovskite community.

In this work, we observed through systematic experimental and computational studies that shallow iodine interstitial defects (I_i) can be unintentionally generated during commonly used surface treatments for state-of-the-art perovskite solar cells (PSCs). Although shallow and, thus, not particularly detrimental to initial device performance, I_i aggravates the phase instability of $FAPbI_3$ perovskites to accelerate its degradation. A universal strategy is proposed to resolve this issue to significantly elongate the operational lifetime of PSCs.

operational stability of the PSCs can potentially be impacted. Therefore, systematic investigations on the effects of shallow defects are required.

In particular, fewer studies have been done on the formamidinium lead triiodide ($FAPbI_3$) perovskite as compared with the prototypical methylammonium lead triiodide ($MAPbI_3$),[14–17] whereas the vast majority of high-performance PSCs are based on a $FAPbI_3$ dominant composition.[3,4] This is significant because of the different degradation mechanisms between the two—$FAPbI_3$, for instance, phase degrades from the photoactive cubic α-$FAPbI_3$ perovskite phase to the hexagonal non-perovskite δ-$FAPbI_3$ phase, whereas the $MAPbI_3$ perovskite phase degrades into PbI_2.[14,16,18] Point defects disrupt the original lattice arrangement, and thus might affect the thermodynamic energetics of the perovskite,[19,20] especially relevant for $FAPbI_3$ because of its metastable nature. Therefore, it is of critical importance to understand the effects of the intrinsic point defects to mitigate the instability issues of $FAPbI_3$-based PSCs.

In this study, we observed that shallow iodine interstitial defects (I_i) can be generated unintentionally during commonly used post-fabrication treatments. We show that I_i can lower the cubic-to-hexagonal phase transformation activation energy barrier of $FAPbI_3$-based perovskites to accelerate its degradation. We demonstrate that concurrently avoiding the generation of I_i and the more effective passivation of iodine vacancy defects (V_I) improves the thermodynamic phase stability and operational stability of the perovskite films and devices. Consequently, our most stable PSC devices demonstrated a more than 5-fold increased average lifetime over the control devices under continuous illumination operational stability testing. The champion device retained 92.1 % of its initial performance after nearly 1,000 h of testing.

RESULTS AND DISCUSSION

Identification of Iodine Interstitial Defects

Iodine-related shallow defects are theoretically predicted to have relatively low (bulk) formation energies.[6–8] Recently, post-fabrication surface treatment strategies using organic iodides have been reported by many groups. The iodide anion (I^-) has been reported to passivate V_I defects.[21–23] However, we speculated that excessive I^- coated on the perovskite surface possibly generates shallow iodine-related defects, so we tried to investigate this by mimicking the surface environments while excluding the organic cation.

All control samples for this study are based on a $FAPbI_3$ composition with 5 mol % of added $MAPbBr_3$ fabricated by a one-step antisolvent quenching method. The as-fabricated perovskite films were then post-treated with different concentrations of pure iodine (I_2) dissolved in isopropanol[3] (hereafter, concentrations given in terms of an equivalent concentration of atomic iodine, see Supplemental Experimental Procedures for clarification) at 5,000 rpm, followed by annealing at 100°C for 5 min. The concentrations and deposition conditions were set to be comparable with those commonly reported for organic iodide salts (Table S1). The control films were treated with blank (pure) isopropanol and underwent the same annealing. PSC devices of architecture indium tin oxide (ITO)/SnO_2/perovskite/spiro-MeOTAD/Au were fabricated without or with surface treatment. We observed that the device photovoltaic parameters, including the open-circuit voltage (V_{OC}), measured in reverse current density-voltage (*J-V*) scan, changed marginally with surface treatment (Figure S1), while the scan direction-dependent *J-V* hysteresis (Figures 1A,

[1]Department of Materials Science and Engineering and California NanoSystems Institute, University of California, Los Angeles, Los Angeles, CA 90095, USA

[2]Department of Physics, Marmara University, 34722, Ziverbey, Istanbul, Turkey

[3]Center for Materials Research, Washington State University, Pullman, WA 99164, USA

[4]Department of Materials Science and Engineering, National Chiao Tung University, Hsinchu 30010, Taiwan

[5]Division of Chemistry and Chemical Engineering, California Institute of Technology, Pasadena, CA 91125, USA

[6]SKKU Advanced Institute of Nanotechnology (SAINT) and Department of Nanoengineering, Sungkyunkwan University, Suwon 16419, Republic of Korea

[7]Lead Contact

*Correspondence: ilhan.yavuz@marmara.edu.tr (I.Y.), jw.lee@skku.edu (J.-W.L.), yangy@ucla.edu (Y.Y.)

https://doi.org/10.1016/j.joule.2020.08.016

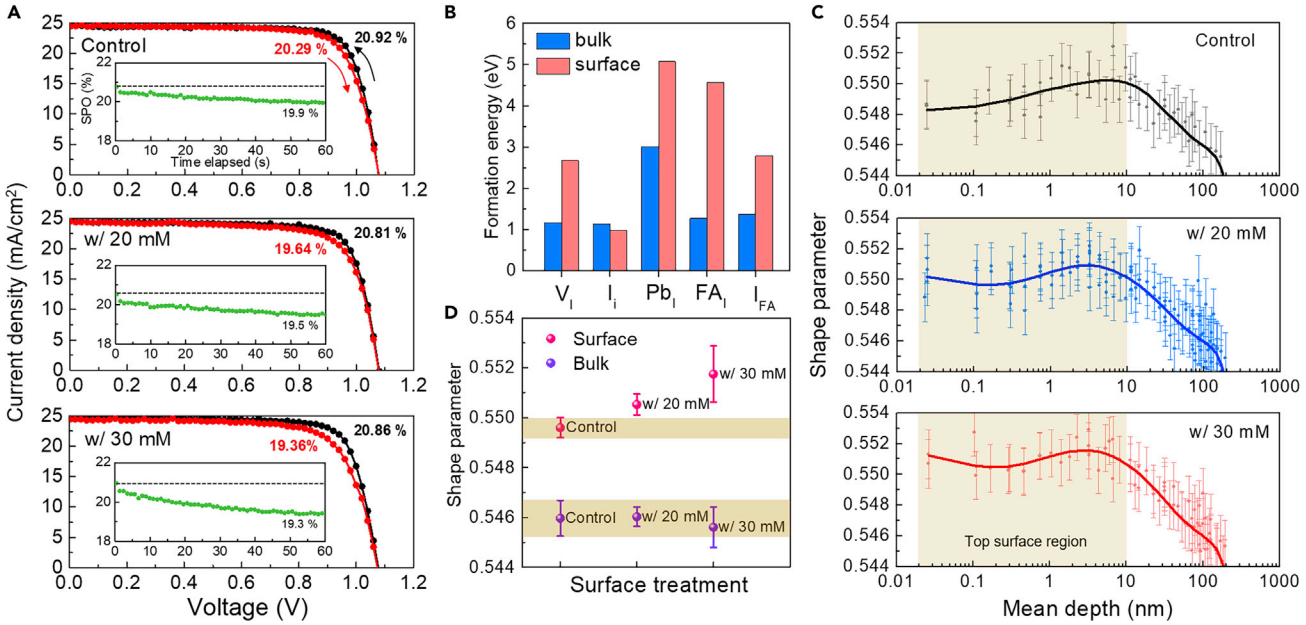

Figure 1. Experimental and Theoretical Indications of Iodine Interstitial Defects

(A) Current density and voltage (J-V) curves of the control and treated devices in reverse (1.2 to −0.1 V) and forward (−0.1 to 1.2 V) scans. Insets are the SPO measurements of the corresponding devices. A horizontal gray line marks the initial SPO.

(B) Bulk and surface formation energies of neutral iodine-related point defects in $FAPbI_3$ perovskite. Bulk values reproduced from Liu and Yam.[7]

(C) PAS depth-profiling of the control and treated perovskite films on glass. Solid lines are fitted plots. Yellow shaded areas indicate the top surface region of the films.

(D) Extracted surface and bulk shape parameters of the perovskite films. Yellow shaded areas demarcate the upper and lower bounds for the control.

S1, and S2) of the devices became increasingly more pronounced. This hints at the formation of shallow iodine-related defects, given that defect migration is responsible for the hysteresis behavior in perovskites.[10,11,24] Particularly, on the longer timescales of the stabilized power output (SPO) measurements (insets of Figure 1A), where defects have sufficient time to migrate and screen the applied bias,[10,25] the SPO is seen to stabilize slower and decays to a lower value with increased surface treatment concentration.

First-principles density functional theory (DFT) calculations were performed to identify the probable defect species. The surface formation energies (Figure 1B) of iodine-related neutral point defects were computed for $FAPbI_3$ grown in stoichiometric conditions for a FAI terminated surface (most thermodynamically stable, see Figure S3 and Supplemental Experimental Procedures for details) and compared with the bulk formation energies reproduced from a previous report.[7] Figure 1B shows that the bulk formation energies of V_I, I_i, FA-I antisite defects (FA_I), and I-FA antisite defects (I_{FA}) are approximately comparable at ~1 eV. The trend, however, changes dramatically at the surface. The calculated formation energies increased from their bulk values for V_I (1.16 to 2.71 eV), FA_I(1.27 to 4.56 eV), and I_{FA} (1.37 to 2.78 eV) but decreased for I_i (1.13 to 0.97 eV). The Fermi-level (E_F) dependence of the formation energies at the surface was further computed for I_i^q, where q denotes the defect charge state (Figure S4). Negatively charged I_i^- has the lowest formation energy across the band gap among the different I_i^q charged states. Near the valence band maximum, the formation energies for I_i^0 and I_i^- are comparable and relatively low at ~1 eV. The position of the (q/q') transitions (transition levels) in relation to the band gap determines the susceptibility of the defect to trap or release charge carriers, i.e., the depth of the (shallow or deep) trap state. The (0/−1) transition occurs

0.03 eV above the valence band edge, whereas the (+1/0) and (+1/−1) transitions occur within the valence band, indicating that I_i is a shallow hole trap with low formation energy. The theoretical results suggest that I_i, predominantly in its I_i^- charged state (because of its relatively lower formation energy) is the likely generated species. Additionally, I_i^- has a low migration activation energy,[9,13,25] and is, thus, a plausible candidate to induce the *J-V* hysteresis. We further note that additional concurrent phenomena reported for $MAPbI_3$ might perhaps also explain the benign nature of I_i^-, including kinetic deactivation due to a fast hole trapping and/or de-trapping process.[26]

We further probed the perovskite films by using positron annihilation spectroscopy (PAS) to investigate the existence of the defects. A basic schematic of the measurement mechanism is shown in Figure S5 (with details in the Experimental Procedures and Supplemental Experimental Procedures). Positively charged positrons (antiparticle to the electron) are implanted from the perovskite surface and annihilate with electrons from a free lattice site or after trapping at negatively charged or neutral (but not positive) vacancies and/or interstitial defects to emit two gamma photons.[27–29] The shape (S) parameter is then extracted from the doppler broadening of the gamma spectrum at each implantation depth. The S parameter increases with the increasing density of defect sites.[27,28] Here, we varied the implantation depth of the positron by changing its kinetic energy (E_k) to investigate the depth-dependent defect density. The results show that the S parameter of the films near the top surface (mean depth < 10 nm, shaded in yellow in Figure 1C) is higher with increasing surface treatment concentration, indicating a higher density of negatively charged or neutral defects at the surface region. Notably, an inverse uptick (Figure 1C) right at the top surface (mean depth < 0.2 nm) is observed for the treated films but not the control film. The selective enhancement in defect density and, thus, S parameter at the top surface (E_k < 0.8 keV, mean depth < 0.24 nm) compared with the bulk region (0.8 keV < E_k < 6 keV, 6.73 nm < mean depth < 170 nm) is more obviously seen in Figure 1D.

Together with the theoretical and device results, the selectivity of PAS to detect only negatively charged or neutral defects supports the generation of I_i^-, i.e., I^- occupying an interstitial site. I_3^- occupying an interstitial site is equivalent to the I_i^+ point defect,[26,30] given that I_i^+ consists of one central I^+ bounded by two I^- (coordinating with Pb) on both sides,[30] i.e., the trimer structure of I_3^-. The dripping solution consists of I_3^- in dynamic equilibrium:[3]

$$I_2 + I^- \leftrightarrow I_3^-$$

We, thus, speculate that the I^- can possibly be generated from (1) the evaporation of I_2 upon post-treatment annealing shifts the dynamic equilibrium toward the reactants to form I^- according to *Le Chatelier*'s principle, and/or (2) the thermal decomposition of I_3^- into I^- from the annealing.[31] Further PAS measurements on samples surface-treated without annealing (Figure S6) support this, in that I^- must have been generated from some back reaction, and that I_3^- (I_i^+) cannot be detected by positrons. We can further exclude any post-treatment induced damage (discussed below). Regardless of the source of I^-, the results suggest that surface treatment with organic iodide salts can unintentionally generate shallow I_i^- defects.

Accelerated Phase Degradation Due to Iodine Interstitial Defects

Although the generated I_i seem to not act as non-radiative electronic traps, we speculated that the intrinsic stability of the perovskite might be affected.[32,33] Specifically, it was shown that excess I_2 added to $MAPbI_3$ accelerated its degradation

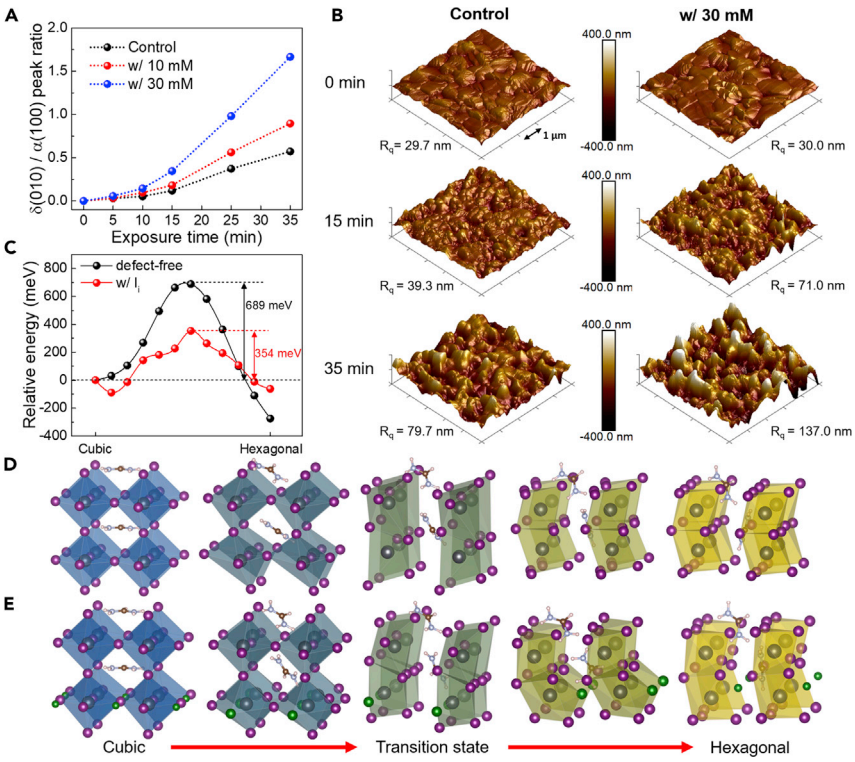

Figure 2. Accelerated Phase Instability of the Treated Perovskite Films

(A) Hexagonal δ(010)-to-cubic α(100) XRD peak intensity ratio of the control and treated perovskite films as a function of exposure time to iodine vapor.

(B) 3D AFM topography images of the control and treated perovskite films after different exposure times to iodine vapor, showing the surface root-mean-square roughness (R_q). Scale bar is 1 μm.

(C) Simulated energy pathway for the cubic-to-hexagonal phase transition with or without I_i defect. The activation energy barriers are included on the right.

(D and E) Evolution of the atomic arrangements for the (D) defect-free and (E) with iodine interstitial (green spheres) lattices during the α-$FAPbI_3$-to-δ-$FAPbI_3$ transformation. Only one unit cell is shown. Atoms are expressed by spheres; iodine (purple), lead (gray), carbon (brown), and nitrogen (blue).

into PbI_2 because of an intrinsic degradation pathway whereby the excess I^- in the perovskite undergoes an autocatalytic chain reaction with self-generated I_2 vapor.[32] Similar degradation by I_2 vapor was also observed for $FAPbI_3$. I_2 vapor inevitably and readily self-forms from within the perovskite[32,33] during PSC operation due to the effect of illumination,[14,33] oxygen,[15] heat,[14,16,33] or even applied bias.[17,34] Importantly, PSC encapsulation cannot fully resolve this intrinsic self-degradation. To test whether surface I_i defects have a similar detrimental role on $FAPbI_3$, we intentionally exposed the perovskite films to I_2 vapor in a nitrogen glovebox as with the previous study.[32]

The phase and morphology evolution of the films were monitored by X-ray diffraction (XRD) and atomic force microscopy (AFM) measurements in Figure 2. The crystallinity, phase purity, morphology, and surface roughness of the fresh films were essentially the same irrespective of surface treatment as seen in Figures 2A, 2B, and S7. The fresh films were dominated by the cubic α-$FAPbI_3$ phase with its characteristic peaks at ~14.1° and ~28.2° corresponding to the (001) and (002) diffraction planes. A small peak at ~12.6° corresponding to the (001) plane of PbI_2 is visible with comparable intensities for all films. After 5 min exposure to I_2 vapor, the intensity of

the α-$FAPbI_3$ peaks decreased with the emergence of a new peak at ~11.8° corresponding to the (010) plane of the hexagonal δ-$FAPbI_3$ non-perovskite phase. With increased exposure to I_2 vapor, the α-$FAPbI_3$ phase incrementally degraded into the δ-$FAPbI_3$ phase. The PbI_2 peak intensity remained approximately unchanged, highlighting a different degradation pathway compared to $MAPbI_3$.[32] Notably, the PbI_2 peak intensity is comparable for all films even after the 35 min exposure. Figure 2A plots the evolution of the δ(010):α(100) peak ratios for the films with exposure time. We observed that the films degraded more rapidly with increased surface treatment concentration. This is supported by the 3D AFM topography images of Figure 2B. All the fresh films were compact and uniform with grain sizes on the order of ~1 μm. The surface root-mean-square roughness (R_q) of the fresh films were comparable (~30 nm). With increased exposure, R_q of the 30 mM treated film was observed to increase more rapidly than the control film, most likely due to an accelerated recrystallization (phase transition) into the δ-$FAPbI_3$ phase: R_q of the treated film increased to 71.0 and 137.0 nm after 15 min and 35 min exposure, respectively. In contrast, R_q of the control film increased from 29.7 to 39.3 to 79.7 nm over the same time period.

The accelerated degradation of cubic α-$FAPbI_3$ without forming PbI_2 suggests that the activation energy barrier for the α-$FAPbI_3$-to-δ-$FAPbI_3$ phase transformation is lowered by the presence of I_i. Given that the phase transformation rate is exponentially proportional to the negative of the activation barrier,[35,36] we performed first-principles calculations to check for any changes in the transition energetics for the α-to-δ phase transformation of $FAPbI_3$ (Figure 2C). Indeed, the results show that the activation barrier nearly halves from 689 to 354 meV with I_i as compared to the defect-free case, correlating with the experimental observations. Therefore, the surface I_i defects probably acted as preferred initiation points for the nucleation of the δ-$FAPbI_3$ phase, which then propagate into the perovskite bulk to accelerate its degradation. A possible origin for the lowered transition barrier can be seen in the intermediate bond reconstruction processes between the defect-free and defected structures (Figures 2D and 2E), where I_i diffuses to participate in the active breakage and reformation of the lattice. This is further seen in the transition states in Figures 2E and S8, where I_i coordinates with Pb in a face-sharing configuration, which is characteristic of the hexagonal crystal structure.[37]

A Possible Mitigation Strategy

In addition to the accelerated phase degradation, although shallow defects (e.g., I_i) by nature do not trap charges, the migration and accumulation of shallow defects at the opposite contact layers can screen the built-in electric field to negatively impact the device performance.'[38,39] In the longer term, shallow defects can possibly penetrate into the adjacent contact layers to induce irreversible chemical reactions.'[40,41] Given the possible generation of I_i from depositing I^- at the perovskite surface during typical surface treatments, a solution would be to replace I^- with an alternative anion. Ammonium iodide salts are usually synthesized via the neutralization reaction between an amine and hydroiodic acid. An alternative acid, which would be deprotonated to its conjugate base on neutralization, is thus the obvious choice. Our initial screening identified trifluroacetate (TFA^-) as a possible choice, given that the pK_a of trifluroacetic acid (0.23) is sufficiently low to ensure that it reacts completely with most common amines.[42] I^- as a counter anion functions to passivate iodine vacancy (V_I) defects.[21–23] Thus, the most crucial requirement for TFA^- is to fulfill the same role.

To assess this possibility, the density of states (DOS) of the defect-free, defected, and passivated surfaces are calculated as in Figure S9. With TFA^-, the electronic states formed by V_I is almost completely eliminated to restore the DOS profile of

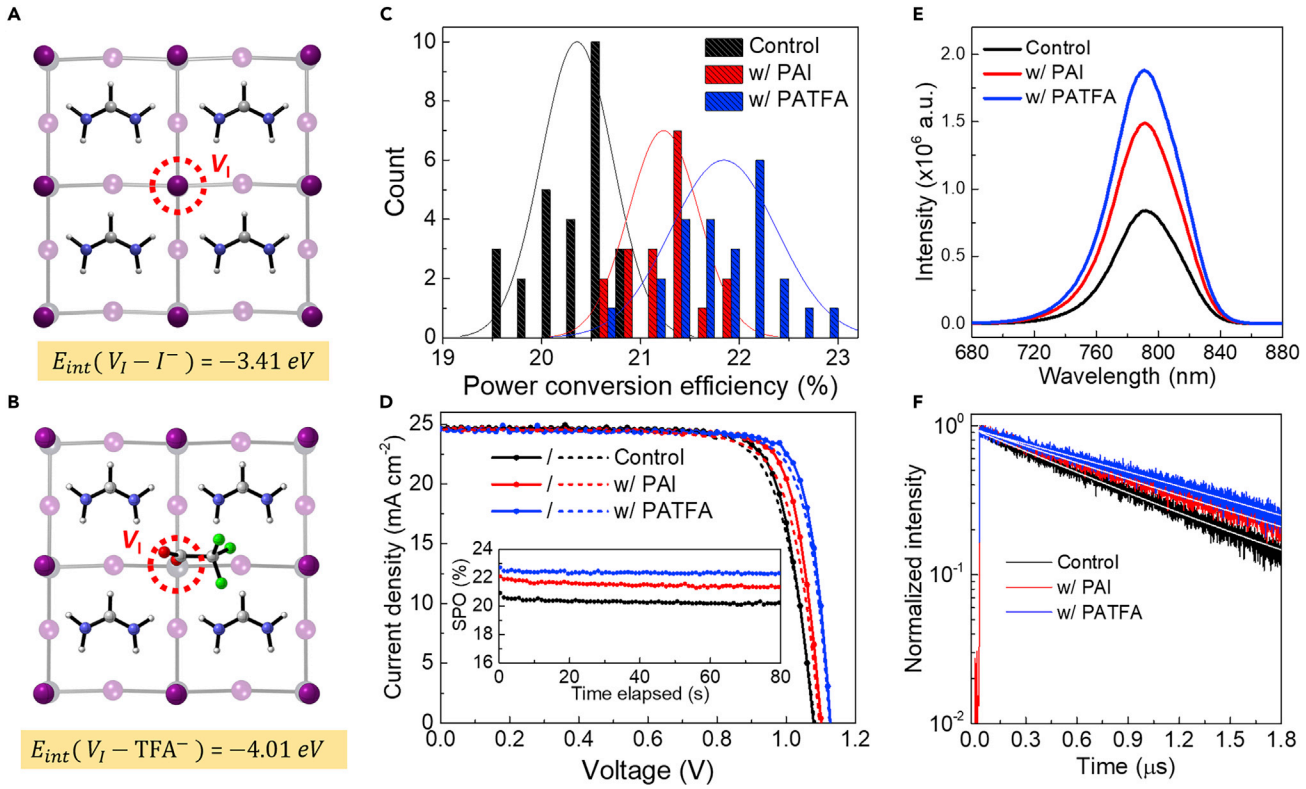

Figure 3. Device Performance and Photoluminescence Properties of the Control and Treated Perovskites

Top view of the slab models used for the (A) V_I - I^- and (B) V_I - TFA interaction energy (E_{int}) calculations. Only the first and second (blurred) layers of the slab are shown. Atoms are expressed by spheres; iodine (purple), carbon (gray), nitrogen (blue), oxygen (red), and fluorine (green).

(C) Power conversion efficiency (PCE) distribution of the control and treated devices.

(D) Current density and voltage (*J-V*) curves of the champion devices in reverse (1.2 to −0.1 V) and forward (−0.1 to 1.2 V) scan. Inset is the SPO of the champion devices.

(E) Steady-state photoluminescence (PL) spectra of the perovskite films on glass probed with an excitation wavelength of 532 nm.

(F) Normalized time-resolved PL spectra of the perovskite films on glass. Solid white lines are the fitted profiles by using a mono-exponential decay function.

the defect-free case. The V_I – TFA^- interaction energy was calculated to be −4.01 eV, higher than the V_I – I^- interaction energy of −3.41 eV (Figures 3A and 3B), suggesting that TFA^- likely passivates V_I more effectively.

To verify our theoretical results, PSC devices were fabricated where the perovskite was post-treated with different ammonium cations. To generalize our approach, an aliphatic (octylammonium, OA), aromatic (phenylammonium, PEA), and zwitterionic (phenylalanine, PA) cation were chosen. The average photovoltaic parameters of the devices are summarized in Table S2. Overall, all treated devices showed superior performance compared that of the control, and all TFA^--treated devices demonstrated higher PCEs attributed to an improved V_{OC} and FF than their corresponding I^- counterparts.

Given that the PA-treated devices demonstrated the best photovoltaic performance, we focused on them to further investigate the differences between I^- and TFA^-. Given that the perovskite surface chemistry might differ when an organic cation capping layer is present,[43] we further probed the perovskite films on glass treated with either PAI or PATFA with PAS (Figure S10). The results show that the S parameter beyond the passivation layer-perovskite interface is higher with PAI

Table 1. Distribution of the Device Photovoltaic Parameters

	V_{OC} (V)	J_{SC} (mA cm^{-2})	FF	PCE (%)	SPO (%)
Control	1.073 ± 0.012 (1.079)	24.45 ± 0.12 (24.67)	0.774 ± 0.012 (0.787)	20.32 ± 0.35 (20.95)	20.3
w/PAI	1.103 ± 0.009 (1.101)	24.49 ± 0.13 (24.62)	0.786 ± 0.014 (0.806)	21.23 ± 0.36 (21.86)	21.4
w/ PATFA	1.120 ± 0.013 (1.127)	24.51 ± 0.10 (24.61)	0.796 ± 0.019 (0.829)	21.84 ± 0.35 (22.98)	22.4

Average photovoltaic parameters of the control and treated devices. Parenthesis indicate parameters measured from champion devices for each condition. Abbreviations are V_{OC}, open-circuit voltage; J_{SC}, short-circuit current density; FF, fill factor; PCE, power conversion efficiency; SPO, stabilized power output.

treatment, supporting the generation of I_i. Further computational calculations (Figure S11) like before on $FAPbI_3$ slabs with PA^+ as a top capping layer[44] indicate that the formation energy for I_i^- (and I_i^0) are more negative (compared with the pristine surface in Figure S3) across the band gap, indicating that its formation is even more energetically favorable. Furthermore, all transition levels occur within the VBM, confirming its shallow nature.

Subsequently, additional devices were fabricated, and the distribution of their photovoltaic parameters are plotted in Figures 3C and S12 and summarized in Table 1. The average PCE of the control devices was increased from 20.32 ± 0.35 % to 21.23 ± 0.36 % with PAI treatment and 21.84 ± 0.35 % with PATFA treatment. The performance enhancement of the treated devices is attributed to an improved V_{OC} (1.073 ± 0.012 to 1.103 ± 0.009 V with PAI treatment to 1.120 ± 0.013 V with PATFA treatment) and FF (0.774 ± 0.012 to 0.786 ± 0.014 with PAI treatment to 0.796 ± 0.019 with PATFA treatment). The J_{SC} of the devices were essentially the same at ~24.5 mA cm^{-2} and well-matched with the external quantum efficiency spectra of the devices with <4 % discrepancy (Figure S13).[45] *J-V* curves of the champion devices are displayed in Figure 3D; individual photovoltaic parameters are summarized in parenthesis in Table 1. The champion PATFA-treated device attained a reverse scan PCE of 22.98 % (J_{SC} of 24.61 mA cm^{-2}, V_{OC} of 1.127 V, and FF of 0.829), higher than that of the PAI-treated device at 21.86 % (J_{SC} of 24.62 mA cm^{-2}, V_{OC} of 1.101 V, and FF of 0.806). The champion control device had a PCE of 20.95 % (J_{SC} of 24.67 mA cm^{-2}, V_{OC} of 1.079 V, and FF of 0.787). The SPOs are included in the inset of Figure 3D and Table 1. The PATFA-treated device achieved a champion SPO of 22.4 %, compared with the 21.4 % and 20.3 % of the PAI-treated and control devices, respectively.

We subsequently measured the steady-state photoluminescence (PL) of the perovskite films on glass to study their carrier recombination dynamics. Excitation wavelengths of 640 and 532 nm were separately used, and the beam incident was on the perovskite side. The excitation wavelength-dependent penetration depths were calculated by using the Beer-Lambert law and the perovskite absorption coefficients (Figure S14). Using the 640 nm excitation source (Figure S15), with an estimated absorption depth of ~200 nm, the steady-state PL peak intensity was minimally enhanced from 1.04 × 10^7 for the control film to 1.08 × 10^7 (3.8% increase) and 1.14 × 10^7 (9.6% increase) for the PAI and PATFA-treated films, respectively. In contrast, using the 532 nm excitation source (Figure 3E), with an estimated absorption depth of ~80 nm and, therefore, more surface sensitive,[46] the peak intensity increased from 8.40 × 10^5 for the control film to 1.49 × 10^6 for the PAI-treated film (77.4 % increase) and 1.88 × 10^6 for the PATFA treated film (123.8 % increase). The

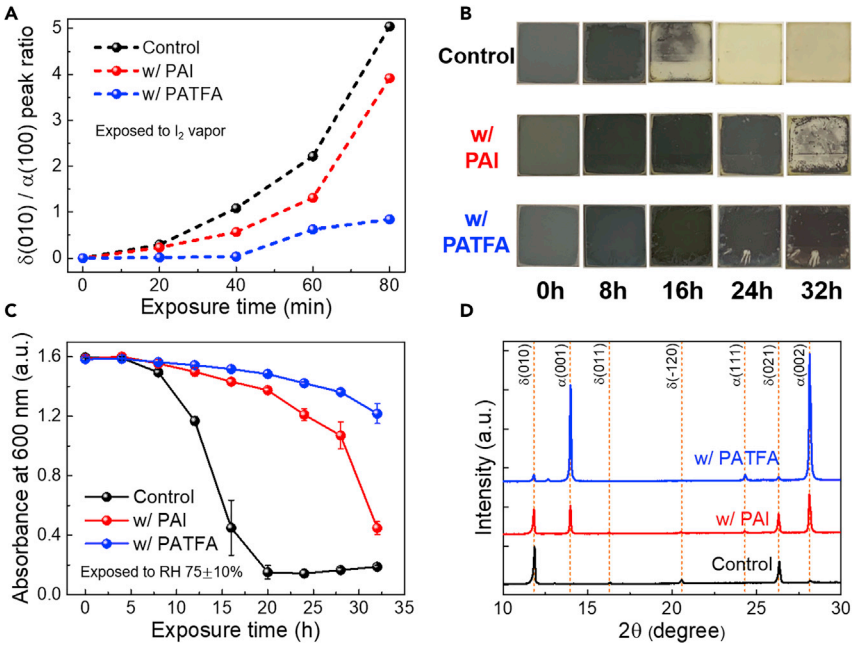

Figure 4. α-Phase Stability of the Control and Treated Perovskite Films

(A) Hexagonal δ(010)-to-cubic α(100) XRD peak intensity ratio of the control and treated perovskite films as a function of exposure time to iodine vapor.

(B and C) (B) Photographs and (C) absorbance at 600 nm of the perovskite films exposed to RH 75 ± 10% with time. d, XRD diffractograms of the perovskite films after exposure to RH 75 ± 10% for 32 h.

excitation wavelength-dependent steady-state PL enhancement confirms that surface treatment of the perovskite films was responsible for their increased radiative recombination. Time-resolved photoluminescence (TRPL) of the films was then measured with the decay profiles fitted with a mono-exponential decay function (Figure 3F). The extracted carrier lifetimes of the films increased from 871 to 1,106 to 1,447 ns for the control, PAI-treated, and PATFA-treated films, respectively. The elongated carrier lifetimes of the treated films indicate suppression of defect-mediated non-radiative recombination and likely contributed to the observed V_{OC} and FF improvements. High-resolution Pb 4*f* X-ray photoelectron spectroscopy (XPS) spectra of the films (Figure S16) indicate that the PATFA-treated film has a stronger interaction with Pb as seen by the peak shifts to higher binding energy, corroborating its theoretically predicted stronger binding with V_I. It might also indicate that TFA^- passivates Pb-related deep traps such as Pb_I antisite defects and/or Pb clusters, which are known to form deep traps in perovskites.[47–49]

α-$FAPbI_3$ Phase Stability of the Perovskite Films

To examine the α-$FAPbI_3$ phase stability of the PA-treated perovskites, we exposed the films to I_2vapor as with before, with the δ(010):α(100) peak ratios extracted from the XRD spectra of Figure S17. As presented in Figure 4A, both PAI or PATFA treatment enhances the α-$FAPbI_3$ phase stability upon exposure to I_2 vapor, but the PATFA treated film proved to be the most stable. After 80 min exposure, the δ(010):α(100) peak ratios of the control, PAI treated and PATFA treated films were 5.04, 3.92, and 0.84, respectively.

To further verify the phase stability, we also exposed the films to a high relative humidity (RH) environment (RH 75 ± 10%), where the α-to-δ phase transformation of

$FAPbI_3$ is also expected to be the dominant degradation mechanism for $FAPbI_3$-based perovskites.[18,50] Photographs of the films with exposure time in 8-h intervals are shown in Figure 4B, and their corresponding absorption spectra were monitored (Figures 4C and S18). We sidenote that the band gaps and absorption profiles of the films remained unchanged with surface treatment. The control film can be visibly seen to degrade completely to the yellow δ-$FAPbI_3$ phase within 24 h of exposure. After 32 h, the PAI-treated film has almost completely degraded to δ-$FAPbI_3$, whereas the black α-$FAPbI_3$ phase of the PATFA-treated film is mostly retained. The average absorbances at 600 nm after 32 h were 0.19, 0.45, and 1.22 for the control, PAI-treated and PATFA-treated films, respectively. This trend was also obvious in the XRD spectra of the films measured after the 32 h exposure, shown in Figures 4D and S19. The characteristic α-$FAPbI_3$ peaks of the PATFA-treated film is still dominant with a comparatively small trace of the δ(010) peak, whereas the α-$FAPbI_3$ peaks of the control film are barely visible. The improved phase stability with PAI treatment is probably due to the defect passivation effects by PA^+ and I^-, evidenced by the improved PL intensity.[46] We speculate that the more improved phase stability of the PATFA-treated films is possibly due to (1) mitigating the unintentional generation of I_i, and (2) the more effective passivation of V_I because of its stronger interaction with TFA^-. We further observed that the average water contact angle, shown in Figure S20, of the PATFA-treated films (73.4 ± 2.8°) is comparable to that of the PAI-treated films (71.8 ± 2.0°). This indicates that the hydrophobicity of the treated films was similar despite the fluorine moiety of TFA^- and as such is likely not the main contributor to the improved phase stability.

Additionally, we investigated the phase stability (and device performance) of the films as a function of PAI concentration (Table S3; Figures S21 and S22). With increasing PAI concentration, the device performance decreases due to noticeable drops in FF and J_{SC}, likely due to a higher series resistance from the thicker (hydrophobic but resistive) capping layer. In contrast, at low PAI concentrations, the phase stability improves due to the thicker hydrophobic capping layer to impede moisture penetration. With even higher PAI concentrations however, we observed aggravated phase instability, which we speculate is due to the generated iodine interstitials outcompeting the thicker capping layer to result in a net worsening of the phase stability. The SPO decayed more rapidly with increasing PAI concentration, likely due to both the thicker capping layer and generated iodine interstitials, but it is difficult to decouple both contributions.

Operational Stability of the Perovskite Solar Cells

To assess the operational stability of the PSCs, encapsulated devices were subjected to continuous illumination at a temperature of ~40°C and under open-circuit condition (see Experimental Procedures for details). In addition to the phase instability of $FAPbI_3$ based PSCs, the migration of ionic defects under the light-induced potential gradient is expected to be the major degradation mechanism during PSC operation.[9,10,50,51] Notably, shallow defects are theoretically predicted to have low migration activation energies.[9,12,25] Defect migration is most severe under open-circuit condition (versus maximum power point tracking) because of the uncompensated built-in potential induced by illumination.[52,53]

Figure 5A plots the evolution of the SPOs of the devices with time. The degradation profiles can be separated into two regimes, where an initial rapid "burn-in" regime for the first ~80 h is subsequently followed by a slower near-linear decay.[10,54,55] The rapid "burn-in" decay was attributed to the redistribution of charged defects, whereas the slower decay was ascribed to irreversible chemical reactions due to

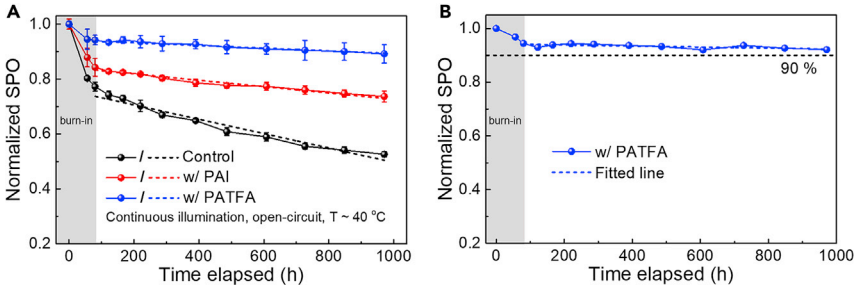

Figure 5. Operational Stability of the Perovskite Devices

(A) Normalized SPO of encapsulated control and treated devices under continuous illumination (90 ± 10 mW cm^{-2}) under open-circuit conditions.

(B) Normalized SPO of the best-performing device with PATFA treatment. Dashed lines are linear fits to extract the device T_{90} lifetime. Shaded areas mark the "burn-in decay" regime.

the migration.[10] The control, PAI-treated and PATFA treated devices retained 77.3 %, 84.3%, and 94.2% of their initial SPOs after the "burn-in" phase, indicating the most reduced defect density with PATFA treatment. Subsequently, the T_{90}, defined as the linearly extrapolated time taken for the SPO to degrade to 90% of its post "burn-in" value,[10,50,54] is obtained by fitting the post burn-in region with an almost linear degradation profile. The average T_{90} of the control devices was enhanced from 383 to 866 h with PAI treatment (126% increase). Even more impressively, the average T_{90} of the PATFA-treated devices was 2,034 h, a 432% and 135% increase over the control and PAI-treated devices, respectively. After 971 h, the devices retained 52.7%, 73.7%, and 89.2% of their initial SPOs for the control, PAI-treated and PATFA-treated devices, respectively. The most stable PATFA-treated device (Figure 5B) retained 92.1 % of its initial SPO after the 971 h testing. The most improved operational stability of the PATFA-treated devices is likely due to (1) avoiding the generation of I_i and (2) more effectively passivating V_I —which are both theoretically predicted to have low migration activation energies[9,12,13] and (3) their superior α-$FAPbI_3$ phase stability.

Conclusion

In this work, through a systematic series of experimental and theoretical results, we unraveled the possible generation of I_i defects at the perovskite surface from commonly used post-fabrication treatments. Regardless of its shallow nature, it was found that I_i accelerates the degradation of $FAPbI_3$-based perovskites by lowering the cubic-to-hexagonal transformation energy barrier. We further demonstrate that concurrently avoiding the generation of I_i and the more effective passivation of V_I by using TFA^- as an alternative counter anion can simultaneously improve the photovoltaic performance, thermodynamic phase stability, and operational stability under continuous illumination of the PSCs. Consequently, our champion PSC devices showed a more than 5-fold increased average T_{90} lifetime over the control devices under operational stability testing. This work sheds light on the detrimental role of shallow defects on the long-term stability of PSCs, highlighting the need to be mindful of them to achieve further stability improvements.

EXPERIMENTAL PROCEDURES

Resource Availability

Lead Contact

Further information and requests for resources and materials should be directed to and will be fulfilled by the Lead Contact, Yang Yang (yangy@ucla.edu).

Materials Availability

This study did not generate new unique materials.

Data and Code Availability

The published article includes all data analyzed and necessary to draw the conclusions of this study in the figures and tables of the main text or Supplemental Information. Further information and requests should be directed to the Lead Contact.

Device Fabrication

Unless otherwise stated, all materials were obtained commercially from Sigma-Aldrich. ITO substrate was cleaned by successive ultrasonication in detergent, deionized water, acetone, and isopropyl alcohol for 20 min each. The cleaned substrate was treated by ultraviolet ozone for 20 min. 0.2 mL of SnO_2 colloidal solution (Alfa Aesar Chemicals) was diluted in 1.2 mL of deionized water and deposited at a rate of 3,000 rpm, followed by annealing at 165°C for 35 min. The prepared SnO_2 film was treated with KOH as previously reported.[56] The substrate was treated with ultraviolet ozone for 20 min. The reference perovskite is based on a previously reported composition[57] by dissolving 889 mg mL^{-1} $FAPbI_3$ (FAI: GreatCell Solar, PbI_2: TCI America), 33 mg mL^{-1} $MAPbBr_3$ (MABr: 1-Material, $PbBr_2$: Alfa Aesar Chemicals), and 33 mg ml^{-1} MACl (GreatCell Solar) in a dimethylformamide (DMF)/dimethylsulfoxide (DMSO) mixed solvent (8:1 v/v). The perovskite was deposited at 4,000 rpm for 20 s, where 0.2 mL of diethyl ether was dropped after 10 s, followed by annealing at 150°C for 10 min. For surface treatment, 15 mM phenylethylammonium-based salts were deposited at 5,000 rpm. 15 mM Octylammonium-based salts were deposited at 5,000 rpm, followed by annealing at 100°C for 5 min. 5 mM Phenylalanine-based salts were deposited at 4,000 rpm followed by annealing at 100°C for 5 min. Then, spiro-MeOTAD solution was prepared by dissolving 85.8 mg of spiro-MeOTAD (p-OLED Corp) in 1 mL of chlorobenzene with 33.8 μl of 4-tert-butylpyridine and 19.3 μl of Li-TFSI (520 mg mL^{-1} in acetonitrile) solution. Spiro-MeOTAD was deposited at 3,000 rpm for 30 s. All processing of the perovskite was done in a glovebox filled with dry air. For the top electrode, 80 nm gold was thermally deposited at an evaporation rate of 0.5 A s^{-1}.

Computational Details

First-Principles Calculations

Computations were carried out based on DFT implemented in the VASP package.[58,59] Exchange-correlation was described by Perdew-Burke-Ernzerhof (PBE)[60,61] generalized gradient approximation. Dispersion correction to the total electronic energies are performed by Grimme's DFT-D3 scheme (with Becke-Johnson damping function).[62,63] A standard frozen-core projector augmented-wave (PAW) method has been utilized for atomic valence-core interactions. Plane-wave basis sets with an energy cut-off of 300 eV and a 4 × 4 × 1 Γ-centered k-point mesh were used for optimizations and further 400 eV and 8 × 8 × 1 k-point mesh were used for single-point calculations. The ionic positions and super-cells were allowed to relax for each optimization calculation.

Prediction of Defect Formation Energy

Formation energies of the surface defects are calculated using the following formula:

$$\Delta H_D^q = E_D^q - E_0 + \sum_i \Delta n_i \mu_i + q(E_F + E_{VBM}),$$

where D and q denotes the defective energy and charge states, respectively. E_0 is the non-defective energy, Δn_i is the number change in element removal (or addition)

to create defect, and μ_i is the corresponding chemical potential. E_F is the Fermi energy and E_{VBM} is the valence-band maximum energy. $\epsilon(q/q')$ are calculated from the matching of the formation energies of two charge states: $\Delta H_D^q(E_F) = \Delta H_D^{q'}(E_F)$. The surface formation energies (with or without organic ammonium capping layer) are calculated on FAI terminated surfaces due to it being the most thermodynamically stable.

Computational Details for Barrier Calculation

The energy landscape of transition pathways from bulk cubic to hexagonal phases without and with bulk defects are obtained by constrained structure optimizations. The structures of the pathways are generated from the linear interpolation consisting of 12 grid points between the initially optimized cubic and hexagonal phases. The energy profiles are then described by a nudged elastic band (NEB) and constrained energy minimization methods implemented in VASP. Energies' barriers are finally computed from the total energy difference between the cubic phase and the saddle points.

Positron Annihilation Spectroscopy

PAS was carried out at the Washington State University positron beam. Monoenergetic positrons with energies selected from 0.02 to 70 keV are transported with a ~180 gauss (0.018 Tesla) to the perovskite samples from a ^{22}Na source isotope-W thin film single crystal moderator. Positrons thermalize rapidly within 5 ps. Annihilations predominantly occur into two near collinearly emitted photons with an average energy of 511 keV. A high-purity high-efficiency Germanium detector with an energy resolution of 1.4 keV with full-width-at-half-maximum (FWHM) at 511 keV is used to detect and energy analyze the deposited energy of the photon. Only events in the photoelectric peaks are considered for the Doppler broadening measurements. The data in the photoelectric peak are area normalized to unit total counts after a suitable background subtraction. The fraction of events collected in a narrow 1.490 keV wide region centered at 511 keV and the two wing regions from 2.61 to 5.87 keV on each side from the 511 keV peak are extracted. They are the shape (S) and wing (W) parameters, respectively. Experiments are carried out in dark. Data analysis is performed with the standard Doppler broadening software called VepFit.[64] Inputs are the values for S with uncertainties at the measured energies. Care is taken to minimize the effects of correlation between layer diffusion lengths and the thickness of the layer.

Synthesis of Ammonium Salts

Phenylethylammonium iodide and Octylammonium iodide were purchased commercially from GreatCell Solar. Phenylalanine iodide was sythesized by adding hydroiodic acid (57 wt % in H_2O) dropwise into phenylalanine and ethanol. The mixture was stirred vigorously for 4 h in an ice bath under argon gas flow. The solvent was then removed using a rotary evaporator and the precipitate was dissolved in ethanol and recrystallized three times in diethyl ether. The phenylalanine iodide crystals obtained by the recrystallization process were then dried at 60°C under vacuum overnight. Phenylalanine iodide had to be synthesized to remove the H_2O solvent from hydroiodic acid. For the trifluroacetate-based salts, the corresponding amine was added to a trifluoroacetic acid (>99.5% EMD Millipore Corp)/isopropyl alcohol mixed solvent, followed by stirring at 50°C overnight. Note that phenylalanine is insoluble in pure isopropyl alcohol, and only the salts phenylalanine iodide or phenylalanine trifluroacetate formed by the neutralization reactions are soluble.

Material Characterization

XRD was performed by an X-ray PANalytical diffractometer at a scan rate of 4° min^{-1} with Cu Kα radiation source. AFM was done using a Bruker dimension Fast Scan with peak-force tapping mode using a 1 ohm silicon tips (OTESPA, Bruker). The photoluminescence (PL) spectra were measured with a Horiba Jobin Yvon system, where a 640 nm monochromatic laser or a 532 nm xenon lamp was used as the excitation source. The time-resolved photoluminescence (TRPL) spectra were measured using a Picoharp 300 with time-correlated single-photon counting capabilities excited by the 640 nm pulse laser diode (PLD 800B, PicoQuant) with a repetition frequency of 200 kHz. Ultraviolet-visible (UV-vis) absorption spectra were recorded by Hitachi U-4100 spectrophotometer equipped with an integrating sphere. X-ray photoelectron spectroscopy (XPS) measurements were carried out on an XPS AXIS Ultra DLD (Kratos Analytical). An Al Kα (1,486.6 eV) X-ray was used as the excitation source.

Device Characterization

A Keithley 2401 source meter was used to measure the current density and voltage curves of the devices under simulated one sun AM 1.5G spectrum illumination (100 mW cm^{-2}) from an Oriel Sol3A class AAA solar simulator (Newport). The light intensity was first calibrated with a NREL-certified Si photodiode with a KG-5 filter. All devices were measured in ambient air with a 0.100 cm^2-sized metal aperture used to precisely define the active area during measurement. Devices were measured at a scan rate of 0.1 V s^{-1} from 1.2 to −0.1 V or 0.1 to 1.2 V in 0.02 V steps. Steady-state power output was calculated by measuring the stabilized photocurrent density at a constantly applied bias. External quantum efficiency (EQE) was measured with a specially designed Enlitech system under AC mode (frequency = 133 Hz) without light bias with a lock-in amplifier with a current preamplifier under short-circuit condition.

Operational Stability Test

Devices were encapsulated inside a glove box filled with nitrogen by using a UV-curable adhesive and a piece of the cover glass. The cover glass was superimposed on the active layer and fixed in position with the UV-curable adhesive. Encapsulated devices were exposed to continuous illumination under open-circuit conditions using an in-house-built aging chamber with a metal-halogen xenon lamp source (90 ± 10 mW cm^{-2}). The chamber atmosphere is in open ambient air (RH 40 ± 10%). Periodically, the devices are transferred to a simulated 1-sun AM 1.5G spectrum illumination from a solar simulator to measure the SPO, also done in ambient air (RH 40 ± 10%). The devices are immediately returned to the aging chamber upon completion.

SUPPLEMENTAL INFORMATION

Supplemental Information can be found online at https://doi.org/10.1016/j.joule.2020.08.016.

ACKNOWLEDGMENTS

This work was supported by the U.S. Department of Energy's Office of Energy Efficiency and Renewable Energy (EERE) under the Solar Energy Technologies Office under award number DE-EE0008751. Computing resources used in this work were provided by the National Center for High-Performance Computing of Turkey (UHEM) with grant number 5005902018. M.H.W. would like to acknowledge the detailed discussions with the late Kelvin G. Lynn. M.H.W.'s contributions and the PAS work was supported by subcontract to Washington State University from the University of California, Los Angeles of a grant by the U.S. Department of Energy's Office of Energy Efficiency and Renewable Energy (EERE) under the Solar Energy

Technologies Office under award number DE-EE0008751 awarded to Dr. Yang Yang. This work was also supported by the National Research Foundation of Korea (NRF) grant funded by the Korea government (MIST) under contract number NRF-2020R1F1A1067223.

AUTHOR CONTRIBUTIONS

S.T., J.-W.L., and Y.Y. conceived the idea, designed most of the experiments, analyzed all the data, and prepared the manuscript. I.Y. and S.N. performed the theoretical calculations, modeling, and analysis. M.H.W. conducted the Positron Annihilation Spectroscopy measurements and analysis. T.H. assisted in experiments and performed the X-ray photoelectron spectroscopy measurements. C.-H.C. performed the chemical synthesis, under the supervision of K.H.W. J.H.K. performed the chemical synthesis. R.W., J.X., and Y.Z. assisted with data analysis and provided helpful discussions. H.-C.W. performed the water contact angle measurements, under the supervision of K.H.W. All authors discussed and commented on the manuscript.

DECLARATION OF INTERESTS

The authors declare no competing interests.

Received: June 14, 2020
Revised: August 4, 2020
Accepted: August 24, 2020
Published: September 23, 2020

REFERENCES

1. Kim, H.S., Lee, C.R., Im, J.H., Lee, K.B., Moehl, T., Marchioro, A., Moon, S.J., Humphry-Baker, R., Yum, J.H., Moser, J.E., et al. (2012). Lead iodide perovskite sensitized all-solid-state submicron thin film mesoscopic solar cell with efficiency exceeding 9%. Sci. Rep. *2*, 591.

2. Yang, W.S., Noh, J.H., Jeon, N.J., Kim, Y.C., Ryu, S., Seo, J., and Seok, S.I.I. (2015). Solar cells. High-performance photovoltaic perovskite layers fabricated through intramolecular exchange. Science *348*, 1234–1237.

3. Yang, W.S., Park, B.W., Jung, E.H., Jeon, N.J., Kim, Y.C., Lee, D.U., Shin, S.S., Seo, J., Kim, E.K., Noh, J.H., and Seok, S.Il (2017). Iodide management in formamidinium-lead-halide-based perovskite layers for efficient solar cells. Science *356*, 1376–1379.

4. Jiang, Q., Zhao, Y., Zhang, X., Yang, X., Chen, Y., Chu, Z., Ye, Q., Li, X., Yin, Z., and You, J. (2019). Surface passivation of perovskite film for efficient solar cells. Nat. Photonics *13*, 460–466.

5. Min, H., Kim, M., Lee, S.U., Kim, H., Kim, G., Choi, K., Lee, J.H., and Seok, S.I.I. (2019). Efficient, stable solar cells by using inherent bandgap of α-phase formamidinium lead iodide. Science *366*, 749–753.

6. Yin, W.-J., Shi, T., and Yan, Y. (2014). Unusual defect physics in CH3NH3PbI3 perovskite solar cell absorber. Appl. Phys. Lett. *104*, 1–4.

7. Liu, N., and Yam, C. (2018). First-principles study of intrinsic defects in formamidinium lead triiodide perovskite solar cell absorbers. Phys. Chem. Chem. Phys. *20*, 6800–6804.

8. Walsh, A., Scanlon, D.O., Chen, S., Gong, X.G., and Wei, S.H. (2015). Self-regulation mechanism for charged point defects in hybrid halide perovskites. Angew. Chem. Int. Ed. Engl. *54*, 1791–1794.

9. Azpiroz, J.M., Mosconi, E., Bisquert, J., and De Angelis, F. (2015). Defect migration in methylammonium lead iodide and its role in perovskite solar cell operation. Energy Environ. Sci. *8*, 2118–2127.

10. Domanski, K., Roose, B., Matsui, T., Saliba, M., Turren-Cruz, S.H., Correa-Baena, J.P., Carmona, C.R., Richardson, G., Foster, J.M., De Angelis, F., et al. (2017). Migration of cations induces reversible performance losses over day/night cycling in perovskite solar cells. Energy Environ. Sci. *10*, 604–613.

11. Lee, J.-W., Kim, S.-G., Yang, J.-M., Yang, Y., and Park, N.-G. (2019). Verification and mitigation of ion migration in perovskite solar cells. APL Mater *7*, 1–12.

12. Aristidou, N., Eames, C., Sanchez-Molina, I., Bu, X., Kosco, J., Islam, M.S., and Haque, S.A. (2017). Fast oxygen diffusion and iodide defects mediate oxygen-induced degradation of perovskite solar cells. Nat. Commun. *8*, 15218.

13. Meloni, S., Moehl, T., Tress, W., Franckevic, M., Saliba, M., Lee, Y.H., Gao, P., Nazeeruddin, M.K., Zakeeruddin, S.M., Rothlisberger, U., and Gratzel, M. (2016). Ionic polarization-induced current–voltage hysteresis in CH3NH3PbX3 perovskite solar cells. Nat. Commun. *7*, 10334.

14. Juarez-Perez, E.J., Ono, L.K., Maeda, M., Jiang, Y., Hawash, Z., and Qi, Y. (2018). Photodecomposition and thermal decomposition in methylammonium halide lead perovskites and inferred design principles to increase photovoltaic device stability. J. Mater. Chem. A *6*, 9604–9612.

15. Aristidou, N., Sanchez-Molina, I., Chotchuangchutchaval, T., Brown, M., Martinez, L., Rath, T., and Haque, S.A. (2015). The role of oxygen in the degradation of methylammonium lead trihalide perovskite photoactiveLayers. Angew. Chem. Int. Ed. Engl. *54*, 8208–8212.

16. Conings, B., Drijkoningen, J., Gauquelin, N., Babayigit, A., D'Haen, J., D'Olieslaeger, L., Ethirajan, A., Verbeeck, J., Manca, J., Mosconi, E., et al. (2015). Intrinsic thermal instability of methylammonium lead trihalide perovskite. Adv. Energy Mater. *5*, 1500477.

17. Yuan, Y., Wang, Q., Shao, Y., Lu, H., Li, T., Gruverman, A., and Huang, J. (2016). Electric-field-driven reversible conversion Between methylammonium lead triiodide perovskites and lead iodide at elevated temperatures. Adv. Energy Mater. *6*, 1–7.

18. Lee, J.-W., Kim, D.-H., Kim, H.-S., Seo, S.-W., Cho, S.M., and Park, N.-G. (2015). Formamidinium and cesium hybridization for photo- and moisture-stable perovskite solar cell. Adv. Energy Mater. *5*, 1–9.

19. Kapur, S.S., Prasad, M., Crocker, J.C., and Sinno, T. (2005). Role of configurational entropy in the thermodynamics of clusters of point

defects in crystalline solids. Phys. Rev. B *72*, 1–12.

20. Bulyarskii, S.V., and Oleinikov, V.P. (1988). Thermodynamics of defect formation and defect interaction in compound semiconductors. Phys. Stat. Sol. (b) *146*, 439–447.

21. Abdi-Jalebi, M., Andaji-Garmaroudi, Z., Cacovich, S., Stavrakas, C., Philippe, B., Richter, J.M., Alsari, M., Booker, E.P., Hutter, E.M., Pearson, A.J., et al. (2018). Maximizing and stabilizing luminescence from halide perovskites with potassium passivation. Nature *555*, 497–501.

22. Li, N., Tao, S., Chen, Y., Niu, X., Onwudinanti, C.K., Hu, C., Qiu, Z., Xu, Z., Zheng, G., Wang, L., et al. (2019). Cation and anion immobilization through chemical bonding enhancement with fluorides for stable halide perovskite solar cells. Nat. Energy *4*, 408–415.

23. Wu, W.Q., Rudd, P.N., Ni, Z., Brackle, C.H. Van, Wei, H., Wang, Q., Ecker, B.R., Gao, Y., and Huang, J. (2020). Reducing surface halide deficiency for efficient and stable iodide-based perovskite solar cells. J. Am. Chem. Soc. *142*, 3989–3996.

24. Tress, W., Marinova, N., Moehl, T., Zakeeruddin, S.M., Nazeeruddin, M.K., and Grätzel, M. (2015). Understanding the rate-dependent J–V hysteresis, slow time component, and aging in CH3NH3PbI3 perovskite solar cells: the role of a compensated electric field. Energy Environ. Sci. *8*, 995–1004.

25. Eames, C., Frost, J.M., Barnes, P.R.F., O'Regan, B.C., Walsh, A., and Islam, M.S. (2015). Ionic transport in hybrid lead iodide perovskite solar cells. Nat. Commun. *6*, 7497.

26. Angelis, F. De, and Petrozza, A. (2018). Clues from defect photochemistry. Nat. Mater. *17*, 377–384.

27. Barthe, M.-F., Labrim, H., Gentils, A., Desgardin, P., Corbel, C., Esnouf, S., and Piron, J.P. (2007). Positron annihilation characteristics in UO_2: for lattice and vacancy defects induced by electron irradiation. Phys. Status Solidi (c) *4*, 3627–3632.

28. Wiktor, J., Jomard, G., Torrent, M., and Bertolus, M. (2017). First-principles calculations of momentum distributions of annihilating electron–positron pairs in defects in UO2. J. Phys. Condens. Matter *29*, 035503.

29. Xue, J., Wang, R., and Yang, Y. (2020). The surface of halide perovskites from nano to bulk. Nat. Rev. Mater. https://doi.org/10.1038/s41578-020-0221-1.

30. Meggiolaro, D., Motti, S.G., Mosconi, E., Barker, A.J., Ball, J., Andrea Riccardo Perini, C.A.R., Deschler, F., Petrozza, A., and Angelis, F. D.e. (2018). Iodine chemistry determines the defect tolerance of lead-halide perovskites. Energy Environ. Sci. *11*, 702–713.

31. Awtrey, A.D., and Connick, R.E. (1951). The absorption spectra of I2, I3-, I-, I03-, S406- and S203=. heat of the reaction I3- = I2 + I-. J. Am. Chem. Soc. *73*, 1842–1843.

32. Wang, S., Jiang, Y., Juarez-Perez, E.J., Ono, L.K., and Qi, Y. (2016). Accelerated degradation of methylammonium lead iodide perovskites induced by exposure to iodine vapour. Nat. Energy *2*, 16195.

33. Fu, F., Pisoni, S., Jeangros, Q., Sastre-Pellicer, J., Kawecki, M., Paracchino, A., Moser, T., Werner, J., Andres, C., Duchêne, L., et al. (2019). I2 vapor-induced degradation of formamidinium lead iodide based perovskite solar cells under heat–light soaking conditions. Energy Environ. Sci. *12*, 3074–3088.

34. Frolova, L.A., Dremova, N.N., and Troshin, P.A. (2015). The chemical origin of the p-type and n-type doping effects in the hybrid methylammonium-lead iodide (MAPbI3) perovskite solar cells. Chem. Commun. (Camb.) *51*, 14917–14920.

35. Han, T.-H., Lee, J.-W., Choi, C., Tan, S., Lee, C., Zhao, Y., Dai, Z., De Marco, N., Lee, S.-J., Bae, S.-H., et al. (2019). Perovskite-polymer composite cross-linker approach for highly-stable and efficient perovskite solar cells. Nat. Commun. *10*, 520.

36. Zhao, Y., Zhu, P., Wang, M., Huang, S., Zhao, Z., Tan, S., Han, T.H., Lee, J.W., Huang, T., Wang, R., et al. (2020). A polymerization-assisted grain growth strategy for efficient and stable perovskite solar cells. Adv. Mater. *32*, e1907769.

37. Chen, T., Foley, B.J., Park, C., Brown, C.M., Harriger, L.W., Lee, J., Ruff, J., Yoon, M., Choi, J.J., and Lee, S.H. (2016). Entropy-driven structural transition and kinetic trapping in formamidinium lead iodide perovskite. Sci. Adv. *2*, e1601650.

38. Calado, P., Telford, A.M., Bryant, D., Li, X., Nelson, J., O'Regan, B.C., and Barnes, P.R.F. (2016). Evidence for ion migration in hybrid perovskite solar cells with minimal hysteresis. Nat. Commun. *7*, 13831.

39. Weber, S.A.L., Hermes, I.M., Turren-Cruz, S.H., Gort, C., Bergmann, V.W., Gilson, L., Hagfeldt, A., Graetzel, M., Tress, W., and Berger, R. (2018). How the formation of interfacial charge causes hysteresis in perovskite solar cells. Energy Environ. Sci. *11*, 2404–2413.

40. Carrillo, J., Guerrero, A., Rahimnejad, S., Almora, O., Zarazua, I., Mas-marza, E., Bisquert, J., and Garcia-belmonte, G. (2016). Ionic reactivity at contacts and aging of methylammonium lead triiodide perovskite solar cells. Adv. Energy Mater. *6*, 1502246.

41. Besleaga, C., Abramiuc, L.E., Stancu, V., Tomulescu, A.G., Sima, M., Trinca, L., Plugaru, N., Pintilie, L., Nemnes, G.A., Iliescu, M., et al. (2016). Iodine migration and degradation of perovskite solar cells enhanced by metallic electrodes. J. Phys. Chem. Lett. *7*, 5168–5175.

42. Milne, J.B., and Parker, T.J. (1981). Dissociation constant of aqueous trifluoroacetic acid by cryoscopy and conductivity. J. Solut. Chem. *10*, 479–487.

43. Yoo, J.J., Wieghold, S., Sponseller, M.C., Chua, M.R., Bertram, S.N., Hartono, N.T.P., Tresback, J.S., Hansen, E.C., Correa-Baena, J.-P., Bulović, V., et al. (2019). An interface stabilized perovskite solar cell with high stabilized efficiency and low voltage loss. Energy Environ. Sci. *12*, 2192–2199.

44. Zheng, X., Chen, B., Dai, J., Fang, Y., Bai, Y., Lin, Y., Wei, H., Zeng, X.C., and Huang, J. (2017). Defect passivation in hybrid perovskite solar cells using quaternary ammonium halide anions and cations. Nat. Energy *2*, 1–9.

45. Wang, H.-C., Chen, C.-H., Li, R.-H., Lin, Y.-C., Tsao, C.-S., Chang, B., Tan, S., Yang, Y., and Wei, K. (2020). Engineering the core units of small-molecule acceptors to enhance the performance of organic photovoltaics. Sol. RRL. https://doi.org/10.1002/solr.202000253.

46. Yang, S., Dai, J., Yu, Z., Shao, Y., Zhou, Y., Xiao, X., Zeng, X.C., and Huang, J. (2019). Tailoring passivation molecular structures for extremely small open-circuit voltage loss in perovskite solar cells. J. Am. Chem. Soc. *141*, 5781–5787.

47. Quan, L.N., Ma, D., Zhao, Y., Voznyy, O., Yuan, H., Bladt, E., Pan, J., Arquer, F.P.G. de, Sabatini, R., Piontkowski, Z., et al. (2020). Edge stabilization in reduced-dimensional perovskites. Nat. Commun. *11*, 1.

48. Han, T.H., Tan, S., Xue, J., Meng, L., Lee, J.W., and Yang, Y. (2019). Interface and defect engineering for metal halide perovskite optoelectronic devices. Adv. Mater. *31*, e1803515.

49. Wang, R., Xue, J., Wang, K.L., Wang, Z.K., Luo, Y., Fenning, D., Xu, G., Nuryyeva, S., Huang, T., Zhao, Y., et al. (2019). Constructive molecular configurations for surface-defect passivation of perovskite photovoltaics. Science *366*, 1509–1513.

50. Lee, J.W., Dai, Z., Han, T.H., Choi, C., Chang, S.Y., Lee, S.J., De Marco, N., Zhao, H., Sun, P., Huang, Y., and Yang, Y. (2018). 2D perovskite stabilized phase-pure formamidinium perovskite solar cells. Nat. Commun. *9*, 3021.

51. Bai, S., Da, P., Li, C., Wang, Z., Yuan, Z., Fu, F., Kawecki, M., Liu, X., Sakai, N., Wang, J.T.-W., et al. (2019). Planar perovskite solar cells with long-term stability using ionic liquid additives. Nature *571*, 245–250.

52. Domanski, K., Alharbi, E.A., Hagfeldt, A., Grätzel, M., and Tress, W. (2018). Systematic investigation of the impact of operation conditions on the degradation behaviour of perovskite solar cells. Nat. Energy *3*, 61–67.

53. Nie, W., Blancon, J.C., Neukirch, A.J., Appavoo, K., Tsai, H., Chhowalla, M., Alam, M.A., Sfeir, M.Y., Katan, C., Even, J., et al. (2016). Light-activated photocurrent degradation and self-healing in perovskite solar cells. Nat. Commun. *7*, 11574.

54. Wang, Z., Lin, Q., Chmiel, F.P., Sakai, N., Herz, L.M., and Snaith, H.J. (2017). Efficient ambient-air-stable solar cells with 2D-3D heterostructured butylammonium-caesium-formamidinium lead halide perovskites. Nat. Energy *2*, 17135.

55. Tan, S., Yavuz, I., Marco, N. De, Huang, T., Lee, S.J., Choi, C.S., Wang, M., Nuryyeva, S., Wang, R., Zhao, Y., et al. (2020). Steric impediment of ion migration contributes to improved operational stability of perovskite solar cells. Adv. Mater. *32*, e1906995.

56. Bu, T., Li, J., Zheng, F., Chen, W., Wen, X., Ku, Z., Peng, Y., Zhong, J., Cheng, Y.B., and Huang, F. (2018). Universal passivation strategy to slot-die printed SnO2 for hysteresis-free efficient flexible perovskite solar module. Nat. Commun. *9*, 4609.

57. Jeon, N.J., Na, H., Jung, E.H., Yang, T.-Y., Lee, Y.G., Kim, G., Shin, H.-W., Il Seok, S.I.I., Lee, J., and Seo, J. (2018). A fluorene-terminated hole-transporting material for highly efficient and stable perovskite solar cells. Nat. Energy *3*, 682–689.

58. Kresse, G., and Furthmüller, J. (1996). Efficiency of ab-initio total energy calculations for metals and semiconductors using a plane-wave basis set. Computational Materials Science *6*, 15–50.

59. Kresse, G., and Furthmüller, J. (1996). Efficient iterative schemes for ab initio total-energy calculations using a plane-wave basis set. Phys. Rev. B Condens. Matter *54*, 11169–11186.

60. Perdew, J.P., Burke, K., and Ernzerhof, M. (1996). Generalized gradient approximation made simple. Phys. Rev. Lett. *77*, 3865–3868.

61. Perdew, J.P., Ruzsinszky, A., Csonka, G.I., Vydrov, O.A., Scuseria, G.E., Constantin, L.A., Zhou, X., and Burke, K. (2008). Restoring the density-gradient expansion for exchange in solids and surfaces. Phys. Rev. Lett. *100*, 136406.

62. Grimme, S. (2006). Semiempirical GGA-type density functional constructed with a long-range dispersion correction. J. Comput. Chem. *27*, 1787–1799.

63. Grimme, S., Antony, J., Ehrlich, S., and Krieg, H. (2010). A consistent and accurate ab initio parametrization of density functional dispersion correction (DFT-D) for the 94 elements H-Pu. J. Chem. Phys. *132*, 154104.

64. Schut, H., van Veen, A., van de Walle, G.F.A., and van Gorkum, A.A.v. (1991). Positron beam defect profiling of silicon epitaxial layers. J. Appl. Phys. *70*, 3003–3006.